

SO(2)-Equivariant Downwash Models for Close Proximity Flight

Henry Smith*, Ajay Shankar, Jan Blumenkamp, Jennifer Gielis, Amanda Prorok

Abstract— Multirotors flying in close proximity induce aerodynamic wake effects on each other through propeller downwash. Conventional methods have thus far fallen short of providing adequate 3D force-based models that can be incorporated into robust control paradigms required when designing and deploying dense flight formations. Thus, *learning* a model for these aerodynamic downwash patterns presents an attractive solution. However, given the computational cost and inadequacy of downwash field simulators for real-world flight settings, data collection for training is confined to real-world experimentation, enforcing the need for sample efficient methods. In this paper, we leverage the latent geometry (e.g., symmetries) present in the downwash fields to accurately and efficiently learn models for the experienced exogenic forces. Using real world experiments, we demonstrate that our geometry-aware model provides improvements over comparable baselines, even when the model is 1/35th the size and has access to a third of the training data.

I. INTRODUCTION

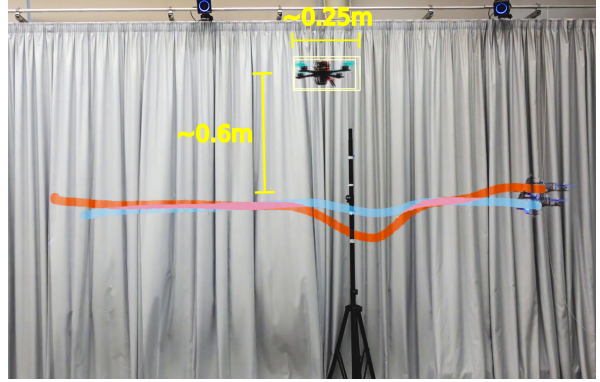
Multi-robot tasks often require aerial robots to fly in close proximity to each other. Such situations occur during collaborative mapping and exploration missions, which may require the robots to navigate constricted areas [1], [2], or when the task is constrained in a more limited workspace from the outset (e.g., indoors) [3]. In some cases, such as aerial docking and payload transport [4], [5], [6], a close approach to another multirotor may indeed be intended. However, the aerodynamic interference experienced by the multirotors poses constraints on the planning of the vehicles' trajectories. Having a model for these exogenic forces could allow for the development of controllers robust to these disturbances, facilitating dense deployments. While it is possible to extract computational fluid models for multirotors that capture aerodynamic interactions over the entire state-space of the problem, such high-fidelity models [7], [8] are often too expensive and restrictive (computational time and run-time memory), or simply unnecessary (dynamically transitioning flight modes). To enable complex and fluid flight missions, we require a fast and accurate representation of the aerodynamic forces experienced by a multirotor when it is in close proximity to another multirotor. Learning representations for these forces that can be evaluated online with a sufficient accuracy onboard the robots can, thus, be more easily embedded in a control and estimation pipeline.

In this work, we present a learning-based approach for estimating the downwash model. Since data collection for

Authors are with the Department of Computer Science & Technology, University of Cambridge, United Kingdom. Emails: {hds35, as3233, jb2270, jag233, asp45}@c1.cam.ac.uk.

* Corresponding author.

This work was supported by ARL DCIST CRA W911NF-17-2-0181, European Research Council (ERC) Project 949940 (gAIa), and, in part, by a gift from Arm.



training is confined to real-world trials, we develop an *equivariant representation* for data-efficient learning. Instead of naively capturing model deviations and attempting to learn them as exogenic forces, we perform a transform that exploits downwash-specific geometric priors. We prove that our model satisfies the assumed $SO(2)$ -equivariant structure of the problem and then use it to learn downwash forces over this transformed domain. This novel model formulation allows us to represent downwash patterns more accurately and efficiently. Our approach collects training sequences by letting the multirotors fly in various formations using a baseline optimal model-based controller (a linear quadratic regulator, LQR). We deploy this model online during flight to collect more experiences at increasingly closer proximities to improve this model over more challenging flight regimes.

A. Related Work

Multi-UAS Flights.

Despite recent and increasing interest in the problem of tight formations in aerial swarms [9], there is a dearth of work that attempts to *deploy* teams in close proximity. This is in-part due to the computational complexity of modeling the fluid aerodynamic interactions between multirotors.

Downwash-induced forces, and the resulting deviations from planned trajectories, are most commonly implicitly corrected for by enforcing hard and large (w.r.t vehicle dimensions) inter-agent separations that minimize the scale of such forces to the point that they can be ignored [10]; allowing the motion planner to use simplified vehicle models. Such approaches severely limit achievable swarm density by naively excluding navigable airspace, and worse may fail to achieve their intended aim due to the chaotic and directional nature of both single- and multi-agent aerodynamic interactions [11], [12].

Recent work combines a physics-based nominal dynamics model with learned deep neural networks to predict down-

wash caused by nearby multirotors as well as ground effects [13], [14]. The proposed approach counteracts predicted forces within an interaction-aware nonlinear stable controller. The authors achieve this for a group of up to five Crazyflie quadrotors. However, the neural network architecture does not make any assumptions about the problem geometry, and is therefore lacks in sample efficiency.

Geometric Deep Learning. Geometric deep learning is a burgeoning research area that interfaces classical machine learning and algebra. At its core, geometric deep learning involves imposing inductive biases on the learning algorithm via one’s knowledge of the problem geometry. In the case of geometric deep learning, these inductive biases are referred to as “geometric priors.” As we will discuss in Section III, these geometric priors are represented using invariance and equivariance assumptions on the underlying function that one wishes to learn [15], [16], [17].

The concept of encoding known geometric information into neural network architectures was first implemented by the *G*-convolution [18] and Steerable [19] convolutional neural networks (CNNs). Since the development of these models, there has been a proliferation of geometric CNNs [20], [21], [22], [23], [24] and graph neural networks (GNNs) [15], [25], [26], [27], [28], among other architectures. The recent popularity of geometric deep learning is due primarily to gains in sample efficiency that geometric priors provide across various application domains [27], [29], [30], [31].

Within the field of robotics, equivariant reinforcement learning has been leveraged to develop low-level controllers for quadrotors [32] and to improve the sample efficiency of grasp learning [33]. Others have demonstrated the efficacy of equivariant deep-*Q* learning and soft actor-critic algorithms in robot manipulation problems [34], [30], [29] and on-robot learning [35]. To our knowledge, there has been no previous work that utilizes geometric priors to efficiently learn multirotor downwash forces.

B. Contributions

The key contributions of our work are as follows:

- 1) We propose an equivariant model for multirotor downwash that takes advantage of the known geometry of the problem. This geometry-aware model represents data in a lower-dimensional space in order to satisfy the known rotational equivariance of our system.
- 2) We provide real-world experimental results that showcase the sample efficiency of our equivariant downwash model. Using only 5 minutes of flight data, we learn the true downwash function with greater accuracy than non-equivariant models do with 15 minutes of data.
- 3) When deployed online within an optimal feedback controller, our model’s predictions are able to reduce vertical tracking errors by over 56 % and lateral tracking errors by nearly 36 %.

II. PROBLEM FORMULATION

Throughout the paper, we consider two identical multirotor vehicles, referred to as *Alpha* (\mathcal{A}) and *Bravo* (\mathcal{B}), operating in close proximity of one another. They have similar estimation

and control stacks onboard, with the only difference being in their reference states/trajectories as well as the additional force correction terms. Without loss of generality, we use *Alpha* as a “leader” aircraft, while *Bravo* is a “follower” and thus frequently suffers under the propeller downwash generated by *Alpha*.

Notation. Unless explicitly specified, we will assume all frames to follow the North-East-Down (NED) convention with a right-hand chirality. We will let $\mathcal{A} = \{a_1, a_2, a_3\}$ denote the body frame of *Alpha* and $\mathcal{M} = \{\hat{e}_1, \hat{e}_2, \hat{e}_3\}$ denote the inertial frame. The matrix $R_{\mathcal{M}}^{\mathcal{C}} \in \text{SO}(3)$ denotes the change-of-basis transformation between the inertial frame \mathcal{M} and a body frame \mathcal{C} . For the case of $\mathcal{C} = \mathcal{A}$, we will abbreviate $R_{\mathcal{M}}^{\mathcal{A}} \equiv R_{\mathcal{A}}$. Note that for any body frame \mathcal{C} , we have $(R_{\mathcal{M}}^{\mathcal{C}})^{\top} = (R_{\mathcal{M}}^{\mathcal{C}})^{-1}$.

Additionally, we will use the notation \mathbf{x} for vectors, and \mathbf{x} for vector-valued functions of time. For an n -dimensional vector \mathbf{x} , we will let $[\mathbf{x}]_i$ to denote its i th component. The position and velocity vectors corresponding to *Alpha* and *Bravo* will be written with the superscripts \mathcal{A} and \mathcal{B} , respectively. We will abbreviate the sine and cosine functions as $s(\cdot)$ and $c(\cdot)$.

Lastly, for the frame of the “leader,” *Alpha*, we define $\text{proj}_{\mathcal{A}} : \mathbb{R}^3 \rightarrow \mathbb{R}^3$ to be the orthogonal projection operator onto the subspace $\mathcal{S}_{\mathcal{A}} \equiv \text{span}\{a_1, a_2\}$. Similarly, we define $\text{proj}_{\mathcal{A}}^{\perp} : \mathbb{R}^3 \rightarrow \mathbb{R}^3$ to be the orthogonal projection operator onto $\mathcal{S}_{\mathcal{A}}^{\perp} = \text{span}\{a_3\}$.

Multirotor Dynamics/Control. We model a multirotor as a rigid body \mathcal{C} with six degrees of freedom with mass m , and dynamics in an inertial NED frame governed by

$$m\mathbf{a} = -R_{\mathcal{M}}^{\mathcal{C}} \cdot T + \hat{e}_3 mg, \quad (1)$$

where T is the collective thrust produced by the rotors and g is the acceleration due to gravity. The matrix $R_{\mathcal{M}}^{\mathcal{C}}$ is composed from the Euler roll (ϕ), pitch (θ) and yaw (ψ) angles of the body in Z-Y-X rotation order. A nominal controller for this system generates the control targets $\mathbf{u} = [\phi, \theta, \dot{\psi}, T]^{\top}$ using a non-linear inversion map on (1) to affect a desired lateral acceleration, $\mathbf{a} \in \mathbb{R}^3$. This allows us to write the system of equations in a linear form,

$$\dot{\mathbf{x}} = A\mathbf{x} + B\mathbf{u}, \text{ and, } y = C\mathbf{x} \quad (2)$$

with $\mathbf{x}(t) = [p_n, p_e, p_d, v_n, v_e, v_d, \psi]^{\top} \equiv [\mathbf{p}, \mathbf{v}, \psi]^{\top}$ representing the state vector, $\mathbf{u}(t) = [a_n, a_e, a_d, \psi]^{\top} \equiv [\mathbf{a}, \psi]^{\top}$ the feedback-linearized control input, and

$$A = \begin{pmatrix} 0_{3 \times 3} & \mathbb{I}_{3 \times 3} & 0_{3 \times 1} \\ 0_{3 \times 3} & 0_{3 \times 3} & 0_{3 \times 1} \\ 0_{1 \times 3} & 0_{1 \times 3} & 0 \end{pmatrix}, B = \begin{pmatrix} 0_{3 \times 3} & 0_{3 \times 1} \\ \mathbb{I}_{3 \times 3} & 0_{3 \times 1} \\ 0_{1 \times 3} & 1 \end{pmatrix}, C = \mathbb{I}_{7 \times 7}.$$

Since (A, B) is controllable, it is then straightforward to derive an optimal stabilizing control law, $\mathbf{u}(t) = -K(\mathbf{x}(t) - \mathbf{x}_r(t))$, that regulates this second-order plant to a reference state \mathbf{x}_r . The gain matrix, K , is designed with a linear quadratic regulator (LQR) to produce a sufficiently high gain margin.

Downwash Model. In this work, we model the aerodynamic downwash effects, $\mathbf{f}_{\text{ext}} \in \mathbb{R}^3$, experienced by a multirotor as additive exogenous forces (or equivalently,

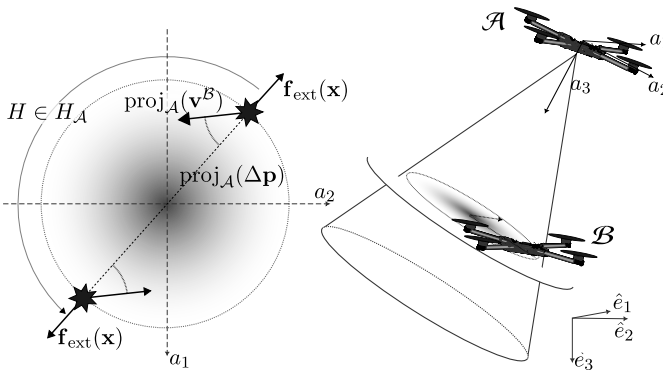


Fig. 1: An illustration of Assumption 2 on the downwash function $\mathbf{f}_{\text{ext}}(\mathbf{x})$. On the left, we provide two combinations of $(\Delta\mathbf{p}, \mathbf{v}^B)$ that are related under the rotational equivariance property.

accelerations) acting on (2). We assume that these forces can be written as $\mathbf{f}_{\text{ext}} \equiv \mathbf{f}_{\text{ext}}(\mathbf{x})$, where $\mathbf{x} = [\mathbf{p}^A, \mathbf{p}^B, \mathbf{v}^A, \mathbf{v}^B]$ contains the instantaneous state information of *Alpha* and *Bravo*. The second-order model described above abstracts the torques produced by per-motor thrust differentials and delegates the regulation of angular states to a well-tuned low-level autopilot. This method of successive loop-closure [36] allows us to model the short-term torque dynamics induced by aerodynamic interactions as collective forces, thereby generalizing the method to other types of aircraft. Hence, (2) can now be rewritten as $\dot{\mathbf{x}} = A\mathbf{x} + B\mathbf{u} + B\mathbf{f}_{\text{ext}} = A\mathbf{x} + B(\mathbf{u} + \mathbf{f}_{\text{ext}})$. Since our control, \mathbf{u} , is designed with very high gain margins, we can use this linear separability to adapt the feedback control to compensate for this effect as $\mathbf{u}_F(t) \equiv -K(\mathbf{x}(t) - \mathbf{x}_r(t)) - \mathbf{f}_{\text{ext}}$. We note that, in the general case where the controller stability margin may be narrow, this compensation can be incorporated through appropriate constraint-based methods (such as model predictive control, MPC).

Problem. Our objective is to learn a data-efficient model that predicts $\mathbf{f}_{\text{ext}}(\mathbf{x})$ such that a closed-loop controller can compensate for predicted exogenous disturbances online.

III. ESTABLISHING GEOMETRIC PRIORS

In order to efficiently and accurately model the downwash forces experienced by *Bravo*, we first make assumptions on the geometry present in $\mathbf{f}_{\text{ext}}(\mathbf{x})$. Our assumptions are formalized using the group-theoretic definitions of invariance and equivariance. Later on, we will impose these assumptions as geometric priors in our learning algorithm.

A. Geometric Invariance and Equivariance

The geometric properties of functions are described in terms of group actions. To be specific, let G be a group and \mathcal{X} be a set. The *action* of group G on set \mathcal{X} is a mapping $\star : G \times \mathcal{X} \rightarrow \mathcal{X}$ which associates with each group element and set element a corresponding set element. The group action \star must satisfy certain properties [15], [16]. In this case, we say that “ G acts on \mathcal{X} according to \star .”

For instance, if $G = \text{SO}(2)$ and $\mathcal{X} = \mathbb{R}^2$, then G can act on \mathcal{X} according to matrix multiplication: $G_\omega \star \mathbf{w} = G_\omega \mathbf{w}$,

where $G_\omega \in \text{SO}(2)$ is the rotation matrix corresponding to the angle $\omega \in [0, 2\pi]$ and $\mathbf{w} \in \mathbb{R}^2$ is an arbitrary vector.¹

Using group actions, one can define *invariant* and *equivariant* functions:

Definition 1 (Invariance, Equivariance). *Let G be a group and \mathcal{X}, \mathcal{Y} be two sets. Suppose that G acts on \mathcal{X} according to \star_1 and on \mathcal{Y} according to \star_2 .*

*A function $f : \mathcal{X} \rightarrow \mathcal{Y}$ is **invariant** with respect to \star_1 if it satisfies*

$$f(x) = f(g \star_1 x), \quad \forall x \in \mathcal{X}, \forall g \in G.$$

*And f is said to be **equivariant** with respect to \star_1 and \star_2 if it satisfies*

$$g \star_2 f(x) = f(g \star_1 x), \quad \forall x \in \mathcal{X}, \forall g \in G.$$

Intuitively, invariance states that the output of f should be preserved regardless of whether or not $g \in G$ acts on the input. Equivariance, on the other hand, states that $g \in G$ acting on the input x according to \star_1 is equivalent to g acting on the output of f , $f(x)$, according to \star_2 .

B. Geometric Assumptions on \mathbf{f}_{ext}

Now that we have detailed the geometric properties a function may have, we consider the particular structure of the interaction forces $\mathbf{f}_{\text{ext}}(\mathbf{x})$ that *Alpha* exerts on *Bravo*.

Foremost, we know that $\mathbf{f}_{\text{ext}}(\mathbf{x})$ should not depend on positional shifts in the input space:

Assumption 1 (Translation Invariance). *Define the group T consisting of all translations in \mathbb{R}^3 . T is isomorphic to \mathbb{R}^3 . And consider the group action \star_1 on the input space defined by $\mathbf{t} \star_1 \mathbf{x} = [\mathbf{t} + \mathbf{p}^A, \mathbf{t} + \mathbf{p}^B, \mathbf{v}^A, \mathbf{v}^B]$ for $\mathbf{t} \in T$. Then we assume $\mathbf{f}_{\text{ext}}(\mathbf{x})$ is invariant with respect to this group action.*

Equivalently, Assumption 1 states that \mathbf{f}_{ext} must be a function of $\Delta\mathbf{p}$, \mathbf{v}^A , and \mathbf{v}^B only. From here on, we will redefine $\mathbf{x} \equiv [\Delta\mathbf{p}, \mathbf{v}^A, \mathbf{v}^B] \in \mathbb{R}^9$. This assumption of translation invariance is standard in downwash prediction models [13] [14].

However, beyond translation invariance, previous downwash models have failed to consider the geometry present in \mathbf{f}_{ext} . In particular, translation invariance does not take into account the fact that, once the downward direction a_3 of the “leader” *Alpha* is fixed, how one defines the north and east directions is arbitrary. That is to say, although we fix a_1 and a_2 to be north and east vectors in the body frame of *Alpha*, our force predictions should not differ if we were to rotate our basis vectors a_1 and a_2 in \mathcal{S}_A by $\omega \in [0, 2\pi]$. This is the subject of the following assumption:

Assumption 2 (Rotational Equivariance). *Define the group $H_A \leq \text{SO}(3)$ containing all rotations that fix a_3 , the down direction in the body frame of *Alpha*:*

$$H_A = \{H \in \text{SO}(3) \mid \text{proj}_A^\perp(H\mathbf{w}) = \text{proj}_A^\perp(\mathbf{w}), \forall \mathbf{w} \in \mathbb{R}^3\}. \quad (3)$$

¹This group action is technically a group representation: an action of G on a vector space by invertible linear transformations.

Notice that $H_{\mathcal{A}}$ is isomorphic to the two-dimensional rotation group, $\text{SO}(2)$. Define the action of $H_{\mathcal{A}}$ on the input space by $H \star_1 \mathbf{x} = [H\Delta\mathbf{p}, \mathbf{v}^{\mathcal{A}}, H\mathbf{v}^{\mathcal{B}}]$ and on the output space by $H \star_2 \mathbf{w} = H\mathbf{w}$, $\mathbf{w} \in \mathbb{R}^3$ for $H \in H_{\mathcal{A}}$. Then we assume $\mathbf{f} = \mathbf{f}(\mathbf{x})$ is equivariant with respect to these group actions.

This rotational equivariance assumption is illustrated in Figure 1. Intuitively, Assumption 2 states that in the frame of the leader vehicle *Alpha*, rotating the relative position vector and the velocity vector of *Bravo* in the $\{a_1, a_2\}$ axes by an angle of $\omega \in [0, 2\pi]$ is equivalent to rotating the force vector $\mathbf{f}_{\text{ext}}(\mathbf{x})$ of *Bravo* by the same angle ω .

IV. GEOMETRY-AWARE LEARNING

Now that we have stated our assumptions on $\mathbf{f}_{\text{ext}}(\mathbf{x})$, we encode them as geometric priors in our learning algorithm.

A. Rotationally Equivariant Model

In order to present our model for $\mathbf{f}_{\text{ext}}(\mathbf{x})$, we must first define a feature mapping $h : \mathbb{R}^9 \rightarrow \mathbb{R}^6$

$$h(\mathbf{x}) = \left(\frac{\text{proj}_{\mathcal{A}}(\Delta\mathbf{p})^\top \text{proj}_{\mathcal{A}}(\mathbf{v}^{\mathcal{B}})}{\|\Delta\text{proj}_{\mathcal{A}}(\Delta\mathbf{p})\|_2 \|\text{proj}_{\mathcal{A}}(\mathbf{v}^{\mathcal{B}})\|_2}, \|\text{proj}_{\mathcal{A}}(\Delta\mathbf{p})\|_2, \|\text{proj}_{\mathcal{A}}(\mathbf{v}^{\mathcal{B}})\|_2, -\hat{e}_3^\top \text{proj}_{\mathcal{A}}^\perp(\Delta\mathbf{p}), -\hat{e}_3^\top \text{proj}_{\mathcal{A}}^\perp(\mathbf{v}^{\mathcal{B}}), \|\text{proj}_{\mathcal{A}}(\mathbf{v}^{\mathcal{A}})\|_2 \right). \quad (4)$$

Note that for any vector $\mathbf{w} \in \mathbb{R}^3$, $-\hat{e}_3^\top \mathbf{w}$ represents the third component of \mathbf{w} .

The mapping $\mathbf{x} \mapsto h(\mathbf{x})$ transforms each input vector \mathbf{x} in Euclidean space into an invariant representation with respect to the action of $H_{\mathcal{A}}$. It does so by separating each of the inputs $\Delta\mathbf{p}$, $\mathbf{v}^{\mathcal{A}}$, and $\mathbf{v}^{\mathcal{B}}$ into its components in the subspaces $\mathcal{S}_{\mathcal{A}}$ and $\mathcal{S}_{\mathcal{A}}^\perp$: $\mathbf{w} = \text{proj}_{\mathcal{A}}(\mathbf{w}) + \text{proj}_{\mathcal{A}}^\perp(\mathbf{w})$, $\forall \mathbf{w} \in \mathbb{R}^3$.

In particular, because the components of $\Delta\mathbf{p}$ and $\mathbf{v}^{\mathcal{B}}$ contained in $\mathcal{S}_{\mathcal{A}}^\perp$, $\text{proj}_{\mathcal{A}}^\perp(\Delta\mathbf{p})$ and $\text{proj}_{\mathcal{A}}^\perp(\mathbf{v}^{\mathcal{B}})$, are unaffected by the action of $H_{\mathcal{A}}$, then our model has the freedom to operate on them arbitrarily. The components contained in $\mathcal{S}_{\mathcal{A}}$, on the other hand, $\text{proj}_{\mathcal{A}}(\Delta\mathbf{p})$ and $\text{proj}_{\mathcal{A}}(\mathbf{v}^{\mathcal{B}})$, are affected by the action \star_1 of $H_{\mathcal{A}}$. Therefore, we only consider the magnitudes of these vectors as well as the angles between them [28], [37]. Formal verifications of these statements are given in the proof of Theorem 1.

While the feature mapping (4) we proposed is invariant with respect to the action of $H_{\mathcal{A}}$, we ultimately want our model for $\mathbf{f}_{\text{ext}}(\mathbf{x})$ to be equivariant with respect to \star_1 and \star_2 . We achieve this by taking into account the polar angle that $\text{proj}_{\mathcal{A}}(\Delta\mathbf{p})$ forms with the positive a_1 axis in the subspace $\mathcal{S}_{\mathcal{A}}$, which we denote by $\varphi(\mathbf{x}) \in [0, 2\pi)$.

Now, for any neural network function $f_{\Theta} : \mathbb{R}^6 \rightarrow \mathbb{R}^2$ with parameters Θ , we can approximate the downwash forces \mathbf{f}_{ext} felt by *Bravo* as $F_{\Theta} : \mathbb{R}^9 \rightarrow \mathbb{R}^3$:

$$F_{\Theta}(\mathbf{x}) = R_{\mathcal{A}}^\top \left([f_{\Theta}(h(\mathbf{x}))]_1 \cdot [s(\varphi(\mathbf{x})), c(\varphi(\mathbf{x}))], [f_{\Theta}(h(\mathbf{x}))]_2 \right). \quad (5)$$

B. Proof of Equivariance

Theorem 1. The model $F_{\Theta}(\mathbf{x})$ proposed in (5) for $\mathbf{f}_{\text{ext}}(\mathbf{x})$ satisfies Assumption 2.

Proof. By Definition 1 of equivariance, we need to prove that for each $H \in H_{\mathcal{A}}$,

$$H \star_2 F_{\Theta}(\mathbf{x}) = F_{\Theta}(H \star_1 \mathbf{x}),$$

where \star_1 and \star_2 are the group actions in Assumption 2.

First, we point out the fact that

$$H_{\mathcal{A}} = \left\{ R_{\mathcal{A}}^\top \begin{pmatrix} c(\omega) & -s(\omega) & 0 \\ s(\omega) & c(\omega) & 0 \\ 0 & 0 & 1 \end{pmatrix} R_{\mathcal{A}} \mid \omega \in [0, 2\pi] \right\}. \quad (6)$$

In other words, each $H \in H_{\mathcal{A}}$ can be parameterized by the angle of rotation $\omega \in [0, 2\pi)$ about the axis a_3 . Let $H = R_{\mathcal{A}}^\top \Omega R_{\mathcal{A}}$, where Ω is the rotation matrix by ω in (6).

As we previously discussed, we will first show that the feature mapping (4) is *invariant* to the action of $H_{\mathcal{A}}$ on the input space, \star_1 . Since H is a rotation which fixes a_3 , then

$$-\hat{e}_3^\top \text{proj}_{\mathcal{A}}^\perp(H\mathbf{w}) = -\hat{e}_3^\top \text{proj}_{\mathcal{A}}^\perp(\mathbf{w}), \quad \forall \mathbf{w} \in \mathbb{R}^3.$$

Also, notice that

$$\text{proj}_{\mathcal{A}}(\mathbf{w}) = \begin{pmatrix} \mathbb{I}_{2 \times 2} & 0 \\ 0 & 0 \end{pmatrix} R_{\mathcal{A}} \mathbf{w}.$$

Thus, for any vector $\mathbf{w} \in \mathbb{R}^3$,

$$\begin{aligned} \text{proj}_{\mathcal{A}}(H\mathbf{w}) &= \begin{pmatrix} \mathbb{I}_{2 \times 2} & 0 \\ 0 & 0 \end{pmatrix} R_{\mathcal{A}} H \mathbf{w} \\ &= \begin{pmatrix} \mathbb{I}_{2 \times 2} & 0 \\ 0 & 0 \end{pmatrix} R_{\mathcal{A}} R_{\mathcal{A}}^\top \Omega R_{\mathcal{A}} \mathbf{w} \\ &= \Omega \text{proj}_{\mathcal{A}}(\mathbf{w}). \end{aligned}$$

Since Ω is a unitary matrix, and the norm and dot product are preserved under unitary transformations, the previous two results imply $h(H \star_1 \mathbf{x}) = h(\mathbf{x})$.

Hence, it only remains to consider the polar angle that $\text{proj}_{\mathcal{A}}(H\Delta\mathbf{p})$ forms with the positive a_1 axis in $\mathcal{S}_{\mathcal{A}}$, written $\varphi(H \star_1 \mathbf{x})$. But $\text{proj}_{\mathcal{A}}(H\Delta\mathbf{p}) = \Omega \text{proj}_{\mathcal{A}}(\Delta\mathbf{p})$ is just $\text{proj}_{\mathcal{A}}(\Delta\mathbf{p})$ rotated by an angle ω . Therefore, we know that

$$\varphi(H \star_1 \mathbf{x}) \equiv \varphi(\mathbf{x}) + \omega \pmod{2\pi}.$$

Let $\Omega_{2 \times 2} \in \mathbb{R}^{2 \times 2}$ be the submatrix formed by the first two rows and columns of Ω . Using our previous congruence,

$$\begin{aligned} \Omega_{2 \times 2} [s(\varphi(\mathbf{x})), c(\varphi(\mathbf{x}))] &= [s(\varphi(\mathbf{x}) + \omega), c(\varphi(\mathbf{x}) + \omega)] \\ &= [s(\varphi(H \star_1 \mathbf{x})), c(\varphi(H \star_1 \mathbf{x}))]. \end{aligned}$$

Altogether, we conclude that

$$\begin{aligned} F_{\Theta}(H \star_1 \mathbf{x}) &= R_{\mathcal{A}}^\top \left(\Omega_{2 \times 2} [f_{\Theta}(h(\mathbf{x}))]_1 \cdot [s(\varphi(\mathbf{x})), c(\varphi(\mathbf{x}))], [f_{\Theta}(h(\mathbf{x}))]_2 \right) \\ &= R_{\mathcal{A}}^\top \Omega \left([f_{\Theta}(h(\mathbf{x}))]_1 \cdot [s(\varphi(\mathbf{x})), c(\varphi(\mathbf{x}))], [f_{\Theta}(h(\mathbf{x}))]_2 \right) \\ &= H R_{\mathcal{A}}^\top \left([f_{\Theta}(h(\mathbf{x}))]_1 \cdot [s(\varphi(\mathbf{x})), c(\varphi(\mathbf{x}))], [f_{\Theta}(h(\mathbf{x}))]_2 \right) \\ &= H \star_2 F_{\Theta}(\mathbf{x}). \quad \square \end{aligned}$$

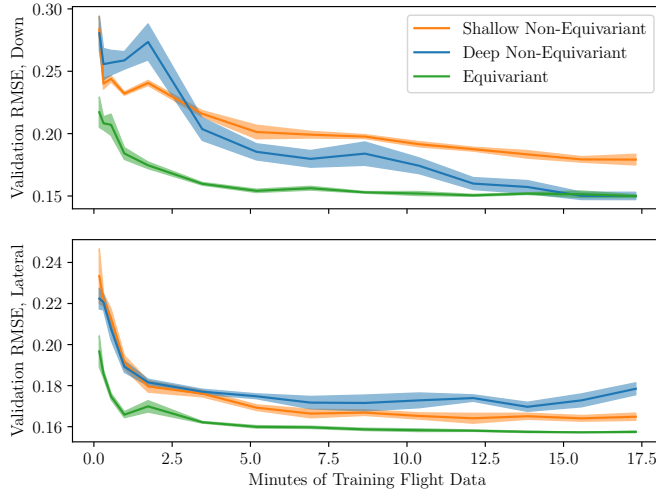


Fig. 2: Sample Efficiency and Accuracy. Top: A visualization of the validation RMSE of the equivariant and non-equivariant models as a function of the training flight time. For each training time, we compute the average validation RMSE across 5 trials. Bottom: Summary statistics for the equivariant and non-equivariant models. Position and velocity tracking errors are reported for models trained on the full training dataset.

C. Shallow Learning

For our training pipeline, we collect time-stamped state and control information from real-world flights with *Alpha* and *Bravo*, and compute the input data points \mathbf{x} offline. The labels that our model (5) learns to approximate are obtained from the feedback control equation (2), $\mathbf{f} = \mathbf{a} - \mathbf{u}(t)$.

We choose the neural network f_Θ in (2) to be a shallow network with a single nonlinear activation

$$f_\Theta(\mathbf{w}) = W^{(2)} \sigma \left(W^{(1)} \mathbf{w} + b^{(1)} \right) + b^{(2)}, \quad \mathbf{w} \in \mathbb{R}^6, \quad (7)$$

where $W^{(1)} \in \mathbb{R}^{32 \times 6}$, $b^{(1)} \in \mathbb{R}^{32}$, $W^{(2)} \in \mathbb{R}^{2 \times 32}$, $b^{(2)} \in \mathbb{R}^2$ are the network parameters Θ and $\sigma(\cdot) = \max(\cdot, 0)$ is the element-wise ReLU nonlinearity. f_Θ is trained to minimize the mean-squared error between the force prediction and label along all three inertial axes $\{\hat{e}_1, \hat{e}_2, \hat{e}_3\}$.

We justify our choice of a shallow neural network architecture via the $\text{SO}(2)$ invariant feature mapping (4). For a neural network trained only on the raw input data \mathbf{x} , the model itself would be responsible for determining the geometries present in \mathbf{f}_{ext} . However, for the equivariant model F_Θ , the feature mapping (4) encodes these geometries explicitly.

Since our equivariant model is not responsible for learning the geometry of \mathbf{f}_{ext} , we can reduce the complexity of f_Θ without sacrificing validation performance. We verify this claim empirically in Section V-B.

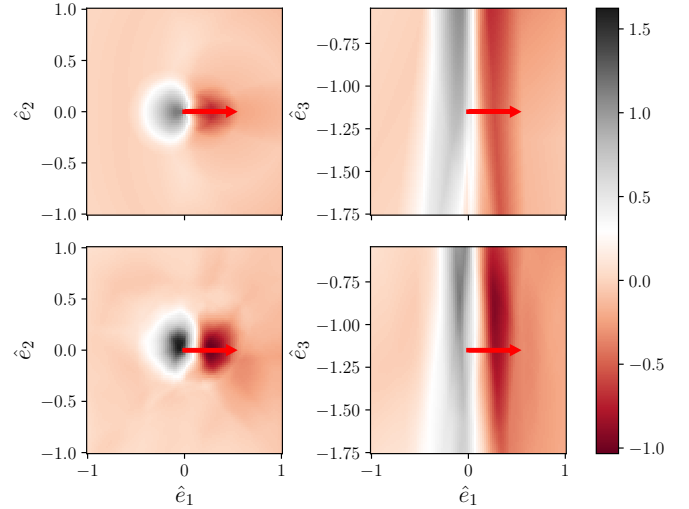


Fig. 3: Downward Force Predictions. Downward force predictions [m/s^2] made by the equivariant model (top) and deep non-equivariant model (bottom). On the left (top-down view), *Alpha* is hovering 1 m above *Bravo* at $(\hat{e}_1, \hat{e}_2) = (0, 0)$. On the right (sagittal view), *Alpha* is hovering 0.1 m east of *Bravo* at $(\hat{e}_1, \hat{e}_3) = (0, 0)$. In each plot, *Bravo* is moving with velocity $\mathbf{v}^B = [0.5, 0, 0]^\top$.

V. REAL-WORLD FLIGHT EXPERIMENTS

We conduct studies with our training procedure and present evaluations from real-world flight experiments. All tests are conducted indoors under partially controlled environments to limit the side-effects of external factors.

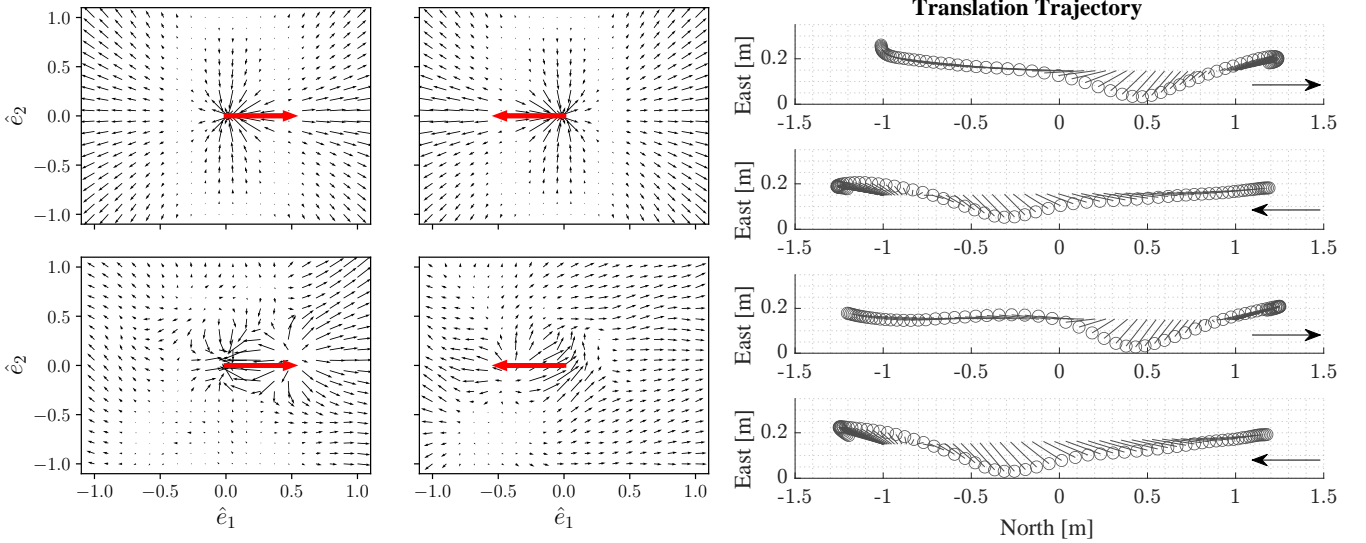
Consequently, we will consider the special case of the model (5) in which $R_A = \mathbb{I}_{3 \times 3}$. In other words, we assume *Alpha*'s frame is a translation of the inertial frame. This special case is realized when *Alpha* is hovering or its instantaneous state is close to hovering. Since the leader's velocity is nearly zero, we omit the component $\|\text{proj}_A(\mathbf{v}^A)\|_2$ from the feature mapping (4).

A. Sequential Data Collection

In order to train our model, we first need to collect a dataset of real-world flights. This is a difficult task, since without a compensation model *a priori*, physical and control limitations will prevent the vehicles from flying in close proximity. To solve this problem, we adopt a sequential approach similar to [13] that splits data collection into different ‘stages’. In stage-0, we fly the vehicles with a relatively large vertical separation, 1.75 m to 1.35 m, so that the forces acting on *Bravo* can be compensated for by a disturbance-rejecting nominal controller.

This controller has no prior knowledge of the exogenous forces, so it simply relies on its feedback control input, $\mathbf{u}(t)$, to track the desired reference trajectories according to (2). However, in regions of strong downwash forces, the measured accelerations, \mathbf{a} will not correspond to the desired acceleration input, \mathbf{u} . These deviations become the computed force labels (represented in mass-normalized acceleration units) for this stage.

After training a stage-0 model using (5), we deploy it online within the control loop such that \mathbf{u}_f now provides the



(a) Lateral force predictions made by the equivariant model (top) and deep non-equivariant model (bottom). On the left, *Bravo* is moving with velocity $\mathbf{v}^B = \text{Alpha}$, without employing a downwash model. The circular markers $[0.5, 0, 0]^\top$, and on the right it is moving with velocity $-\mathbf{v}^B$. Since $\text{SO}(2)$ denote the *Bravo*'s position and the solid lines show its positioning equivariance (Assumption 2) is not explicitly imposed on the non-equivariant model, its force predictions do not satisfy this assumed geometry.

(b) Position tracking errors for *Bravo* when flying a trajectory under *Alpha* with a vertical separation of 0.8 m. *Alpha* is hovering at $(\hat{e}_1, \hat{e}_2) = (0, 0)$.

feedback regulation. As a result, we can now decrease the separation between the vehicles and obtain a new stage-1 dataset along with its labels (the residual disturbances our stage-0 model is unable to account for). The stage-1 dataset is concatenated with the stage-0 dataset and used to train the stage-1 model.

We repeat this process for a total of three stages, so that at stage-2 the drones have a vertical separation of only ≈ 0.5 m. Our full training dataset consists of approximately 17 minutes of flight data. Note that we can always extract the correct force labels at stage- i by logging the model predictions $F_\Theta(\mathbf{x})$ from stage- $(i-1)$ and subtracting these from the control.

B. Study: Model Training

We first study the effect of geometric priors on the learning algorithm for modelling downwash forces $\mathbf{f}_{\text{ext}}(\mathbf{x})$.

Non-equivariant Baselines. In order to analyze the effect of our geometric priors, we must first introduce two models to which we can compare our $\text{SO}(2)$ -equivariant model (5). These “non-equivariant” models should not exploit the known geometry of \mathbf{f}_{ext} delineated in Assumption 2.

The first non-equivariant model we propose has the same architecture as the shallow neural network (7), with the exception that the input to the network is $[\Delta\mathbf{p}, \mathbf{v}^B] \in \mathbb{R}^6$ rather than invariant feature representation $h(\mathbf{x})$. Note that \mathbf{v}^A is not included because of the near-hover assumption that we specified at the beginning of the section.

We also compare our equivariant model against the eight-layer non-equivariant neural network proposed in prior work [13], [14]. During training, we bound the singular values of the weight matrices to be at most 2. This normalization

technique, called “spectral normalization,” constrains the Lipschitz constant of the neural network [13], [14].

Efficiency of Geometric Learning. As we suggested in Section I, the primary benefit of imposing geometric priors on a learning algorithm is that it has been empirically shown to improve sample efficiency [27], [29], [30], [31]. This issue is pertinent within robotics, wherein collecting real-world data is costly in terms of resources, time and availability.

We investigate the sample efficiency of our $\text{SO}(2)$ -equivariant downwash model by considering the validation root mean-squared error (RMSE) as a function of the length of our training flights. We shorten the full training dataset by shortening each stage of data collection proportionally (e.g. a total training time of three minutes corresponds to one minute of flight for each stage). Our validation dataset is roughly equal in size to the full training dataset.

In Figure 2, we observe that although the validation loss of the shallow non-equivariant network plateaus after approximately 10 minutes of training flight data, it cannot represent the downward aerodynamic forces as accurately as the other models (i.e. greater bias). Conversely, while the deep non-equivariant network accurately learns the downward forces, it requires much more training data to do so (i.e. lower sample efficiency). Neither non-equivariant model learns the lateral forces as accurately as the equivariant model.

The equivariant model (5), on the other hand, displays both high sample efficiency and low bias. With only 5 minutes of flight data, it learns the lateral and downward forces more accurately than both non-equivariant models do with 15 minutes of data.

Visualizing Downwash Predictions. In Figure 3, we visualize the force predictions that our equivariant model

$F_\Theta(\mathbf{x})$ makes in the \hat{e}_3 direction. When *Bravo* passes through the downwash region of *Alpha*, there is a highly repeatable pattern in which it is first subjected to a positive force, which pushes it towards the ground, followed by a negative force, which pulls it upwards. The magnitudes of these positive and negative forces are dependent upon (i) *Bravo*'s speed as it passes through the downwash region, and (ii) the distance of *Bravo* from *Alpha* in both $\mathcal{S}_\mathcal{A}$ and $\mathcal{S}_\mathcal{A}^\perp$. The same patterns have been documented by previous downwash models [13].

Our equivariant model also F_Θ uncovers repeatable patterns in the lateral force directions \hat{e}_1 and \hat{e}_2 . When *Bravo* translates laterally underneath *Alpha*, it is first pushed radially outwards, then sucked inwards immediately upon passing under *Alpha*, and lastly pushed radially outwards once it has passed *Alpha*. These inwards forces are strongest when *Bravo* is traveling at a high speed. In Figure 4, we show that the equivariant model's predictions are consistent with the observed deviations of the *Bravo* from its trajectory.

We believe that we are the first to demonstrate these lateral force patterns via a machine learning approach. Notice from Figure 4 that without the assumption of $SO(2)$ -equivariance, the inwards forces are not discernable.

C. Real-World Experiments

We evaluate the performance of our trained equivariant model (5) in two challenging real-world experiments, and contrast it against a baseline controller as well as the deep non-equivariant model. Each model is trained on the full training dataset as described in Section V-A.

Our tests use two identical quadrotor platforms that are custom-built using commercial off-the-shelf parts. These span 0.24 m on the longest body-diagonal, and weigh 0.65 kg (including batteries). Each platform is equipped with a Raspberry Pi 4B (8GB memory) on which we run our control, estimation and model evaluations. The model-based LQG flight control and estimation (2) is performed by *Freyja* [38], while the neural-network encapsulation is done through PyTorch. The controller and the model evaluations are performed at 50 Hz and 45 Hz respectively.

Prior to conducting tests with *Bravo* in motion, we first ensure that a stationary hover under *Alpha* is stable when the model's predictions are incorporated into *Bravo*'s control loop. This is essential to validate empirically that the predictions made by the model do not induce unbounded oscillations on *Bravo*. The table in Figure 2 lists the quantitative results averaged across all our experiments, compared against baseline methods.

Lemniscate Trajectory. We now evaluate the model deployed in a more dynamic scenario where *Bravo* is commanded to follow a lemniscate trajectory ('figure-8') under *Alpha*. This exposes the model to many different regions of the state space, while also requiring *Bravo* to make continuous changes to its accelerations.

Figure 6 shows tracking results from executing one complete period of this trajectory. We observe that deploying our model produces a significant shift in the distribution of both position and velocity errors, measured in the Euclidean norm. Without any model, *Bravo* loses vertical position tracking

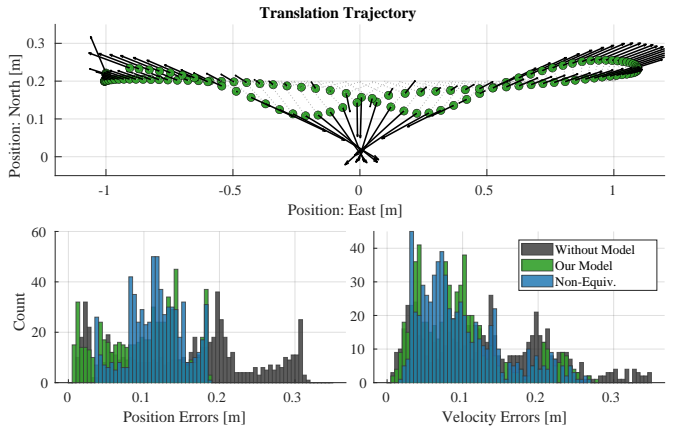


Fig. 5: Translation under *Alpha*. An evaluation of *Bravo*'s flight performance when translating at a fixed altitude beneath *Alpha*. This trajectory is replicated from Figure 4b. Solid black arrows denote the force predictions made by the model. Applying these predictions, our approach decreases the mean position and velocity tracking errors by almost 36 % each (see Figure 2). The gains are greatest along the \hat{e}_3 axis, where the tracking performance is improved by over 55 %.

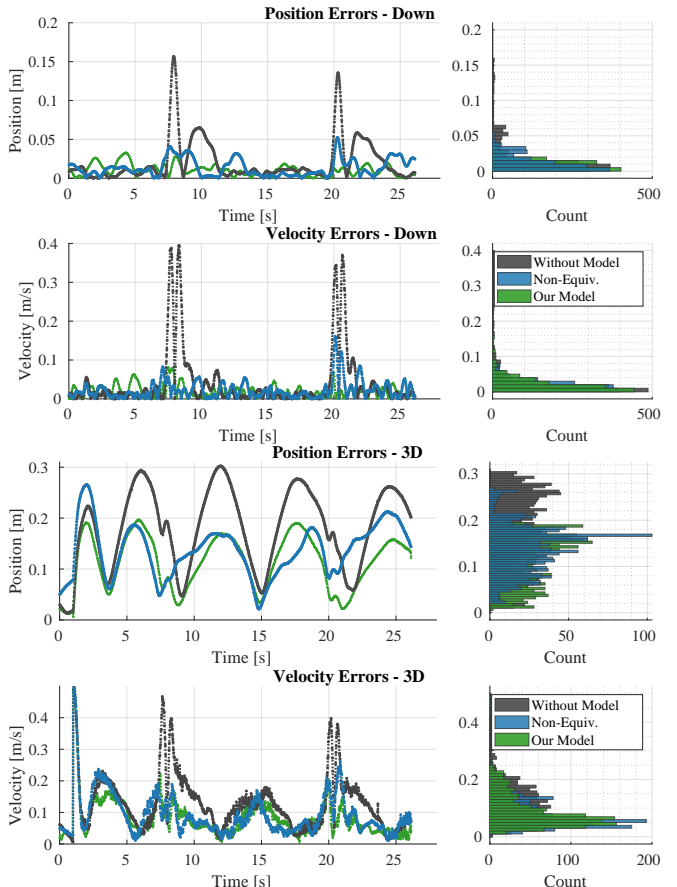


Fig. 6: An evaluation of *Bravo*'s trajectory tracking performance with *Alpha* hovering at $\hat{e}_3 = -2.5$ m. The first two rows show the evolution of the position and velocity tracking errors, as well as their distributions. The last two rows show the same statistics in the 3D space. Compared against a baseline controller (without any model) and a non-equivariant model, our model is able to shrink the distribution of full 3D errors in position (37 % reduction in mean error) and velocity (36 % reduction in mean error). The non-equivariant model only offers 24 % and 28 % reductions, respectively.

(top row) twice as it makes the two passes directly beneath *Alpha*, seen near 8 s and 20 s. These spikes, also noticeable as vertical velocity errors (second row), are “absorbed” due to the predictions made by our equivariant model (as well as the baseline deep non-equivariant model). The equivariant model produces an improvement of nearly 51 % in both position and velocity tracking, whereas the non-equivariant model is still able to provide almost 36 % and 46 % improvement, respectively.

Our model’s ability to represent geometric patterns in the lateral plane is also apparent when considering the full 3D errors (third and fourth rows). The non-equivariant model already improves position tracking by 24 % (0.137 m from 0.181 m) and velocity tracking by nearly 28 % (0.091 m/s from 0.128 m/s). The equivariant model decreases position errors further (down to 0.113 m, 37 % improvement), and also reduces velocity tracking errors (down to 0.081 m/s, a 36 % improvement).

Translation Trajectory Next, we perform an analysis of *Bravo*’s tracking performance and the model’s responses while executing a horizontal transect under *Alpha*. This trajectory is the same as the one shown in Figure 4b, and is useful because it drives *Bravo* rapidly through regions of near-zero to peak disturbances.

Figure 5 illustrates key results from one back-and-forth trajectory parallel to the \hat{e}_2 axis. $\hat{e}_1 = 0.2$ is fixed, and *Bravo* is at a fixed vertical separation of 0.6 m with *Alpha* hovering at $[0, 0, -2.5]$. The first row shows the actual trajectory executed by *Bravo* with our equivariant model deployed (green circles), with an overlay of the force predictions made by the model (solid black arrows). We first point out that the pattern is similar to the one found in Figure 4b, but the peak errors have decreased significantly. Further, the predictions made by our model intuitively correspond to exogenous forces that could potentially cause the pattern of deviations observed. For instance, we observe that at peak deviations ($\hat{e}_1 = 0.1$ m), where *Bravo* has been “pulled in” towards *Alpha*, the force predictions made by the model explain the observed deviations in position.

The distributions of errors shown in the second row demonstrate that the magnitudes of these predictions are also justified. Even though *Bravo* is not directly underneath *Alpha* in these tests, it is still well within *Alpha*’s downwash region. Across experiments, we observe a reduction in the mean 3D positioning error to 0.098 m (from 0.154 m), corresponding to an improvement of almost 36 % (the peak error is also reduced similarly). Velocity tracking error also shows a similar trend, with an average improvement of 34 %. Considering only the vertical tracking performance in these tests (not shown in figures), these statistics jump to 55 % and 49 % (for position and velocity, respectively).

VI. CONCLUSION

This article proposes a data-efficient model for uncovering the downwash forces produced by a single multirotor. Unlike previous learning-based approaches that have tackled this problem [13], [14], we exploit the rotational equivariance of the downwash force function about the vertical axis of

the leader vehicle. This “geometric prior” that we impose on the learning algorithm enables us to first encode our input data into a lower-dimensional space using an invariant feature mapping, before passing it as the input to a neural network.

Through a number of real-world experiments, we demonstrate that our equivariant model outperforms baseline feedback control as well as prior downwash models, especially in regimes where training data is limited. Even more impressively, we demonstrate these improvements with a model that uses a third of the training data and is 1/35th the size of a comparable baseline model.

In the future, we will further explore the potential of our equivariant model through flight regimes with larger force magnitudes. This includes outdoor flights, where the leader and follower can move at sustained greater speeds. Finally, we will generalize our approach to a multi-vehicle system.

ACKNOWLEDGMENT

We thank Peter Woo for his contributions to the construction of the quadrotors and for his helpful discussions throughout the project. We also thank Wolfgang Höning for his clarifications about the sequential data collection procedure employed in [13].

REFERENCES

- [1] J. A. Preiss, W. Honig, G. S. Sukhatme, and N. Ayanian, “Crazyswarm: A large nano-quadcopter swarm,” in *2017 IEEE International Conference on Robotics and Automation (ICRA)*. IEEE, 2017, pp. 3299–3304.
- [2] G. Vásárhelyi, C. Virág, G. Somorjai, T. Nepusz, A. E. Eiben, and T. Vicsek, “Optimized flocking of autonomous drones in confined environments,” *Science Robotics*, vol. 3, no. 20, p. eaat3536, 2018.
- [3] M. Turpin, N. Michael, and V. Kumar, “Trajectory design and control for aggressive formation flight with quadrotors,” *Autonomous Robots*, vol. 33, pp. 143–156, 2012.
- [4] A. Shankar, S. Elbaum, and C. Detweiler, “Dynamic path generation for multirotor aerial docking in forward flight,” in *2020 59th IEEE Conference on Decision and Control (CDC)*. IEEE, 2020, pp. 1564–1571.
- [5] R. Miyazaki, R. Jiang, H. Paul, K. Ono, and K. Shimonomura, “Airborne docking for multi-rotor aerial manipulations,” in *2018 IEEE/RSJ International Conference on Intelligent Robots and Systems (IROS)*. IEEE, 2018, pp. 4708–4714.
- [6] A. Shankar, S. Elbaum, and C. Detweiler, “Multirotor docking with an airborne platform,” in *Experimental Robotics: The 17th International Symposium*. Springer, 2021, pp. 47–59.
- [7] S. Yoon, P. V. Diaz, D. D. Boyd Jr, W. M. Chan, and C. R. Theodore, “Computational aerodynamic modeling of small quadcopter vehicles,” in *American Helicopter Society (AHS) 73rd Annual Forum Fort Worth, Texas*, 2017.
- [8] S. Yoon, H. C. Lee, and T. H. Pulliam, “Computational analysis of multi-rotor flows,” in *54th AIAA aerospace sciences meeting*, 2016, p. 0812.
- [9] S.-J. Chung, A. A. Paranjape, P. Dames, S. Shen, and V. Kumar, “A survey on aerial swarm robotics,” *IEEE Transactions on Robotics*, vol. 34, no. 4, pp. 837–855, 2018.
- [10] X. Zhou, J. Zhu, H. Zhou, C. Xu, and F. Gao, “Ego-swarm: A fully autonomous and decentralized quadrotor swarm system in cluttered environments,” in *2021 IEEE International Conference on Robotics and Automation (ICRA)*, 2021, pp. 4101–4107.
- [11] G. Throneberry, C. Hocut, and A. Abdelkefi, “Multi-rotor wake propagation and flow development modeling: A review,” *Progress in Aerospace Sciences*, vol. 127, p. 100762, 2021. [Online]. Available: <https://www.sciencedirect.com/science/article/pii/S0376042121000658>
- [12] H. Zhang, Y. Lan, N. Shen, J. Wu, T. Wang, J. Han, and S. Wen, “Numerical analysis of downwash flow field from quad-rotor unmanned aerial vehicles,” *International Journal of Precision Agricultural Aviation*, vol. 3, no. 4, 2020.

- [13] G. Shi, W. Höning, Y. Yue, and S.-J. Chung, “Neural-swarm: Decentralized close-proximity multirotor control using learned interactions,” in *2020 IEEE International Conference on Robotics and Automation (ICRA)*. IEEE, 2020, pp. 3241–3247.
- [14] G. Shi, W. Höning, X. Shi, Y. Yue, and S.-J. Chung, “Neural-swarm2: Planning and control of heterogeneous multirotor swarms using learned interactions,” *IEEE Transactions on Robotics*, vol. 38, no. 2, pp. 1063–1079, 2021.
- [15] M. M. Bronstein, J. Bruna, T. Cohen, and P. Veličković, “Geometric deep learning: Grids, groups, graphs, geodesics, and gauges,” *arXiv preprint arXiv:2104.13478*, 2021.
- [16] C. Esteves, “Theoretical aspects of group equivariant neural networks,” *arXiv preprint arXiv:2004.05154*, 2020.
- [17] M. M. Bronstein, J. Bruna, Y. LeCun, A. Szlam, and P. Vandergheynst, “Geometric deep learning: going beyond euclidean data,” *IEEE Signal Processing Magazine*, vol. 34, no. 4, pp. 18–42, 2017.
- [18] T. Cohen and M. Welling, “Group equivariant convolutional networks,” in *International conference on machine learning*. PMLR, 2016, pp. 2990–2999.
- [19] T. S. Cohen and M. Welling, “Steerable cnns,” *arXiv preprint arXiv:1612.08498*, 2016.
- [20] R. Kondor, Z. Lin, and S. Trivedi, “Clebsch–gordan nets: a fully fourier space spherical convolutional neural network,” *Advances in Neural Information Processing Systems*, vol. 31, 2018.
- [21] C. Esteves, C. Allen-Blachette, A. Makadia, and K. Daniilidis, “Learning SO3 equivariant representations with spherical cnns,” in *Proceedings of the European Conference on Computer Vision (ECCV)*, 2018, pp. 52–68.
- [22] T. S. Cohen, M. Geiger, J. Köhler, and M. Welling, “Spherical cnns,” *arXiv preprint arXiv:1801.10130*, 2018.
- [23] M. Weiler and G. Cesa, “General E(2)-equivariant steerable cnns,” *Advances in Neural Information Processing Systems*, vol. 32, 2019.
- [24] T. S. Cohen, M. Geiger, and M. Weiler, “A general theory of equivariant cnns on homogeneous spaces,” *Advances in neural information processing systems*, vol. 32, 2019.
- [25] I. Batatia, D. P. Kovács, G. N. Simm, C. Ortner, and G. Csányi, “Mace: Higher order equivariant message passing neural networks for fast and accurate force fields,” *arXiv preprint arXiv:2206.07697*, 2022.
- [26] J. Brandstetter, R. Hesselink, E. van der Pol, E. J. Bekkers, and M. Welling, “Geometric and physical quantities improve E(3) equivariant message passing,” *arXiv preprint arXiv:2110.02905*, 2021.
- [27] S. Batzner, A. Musaelian, L. Sun, M. Geiger, J. P. Mailoa, M. Kornbluth, N. Molinari, T. E. Smidt, and B. Kozinsky, “E(3)-equivariant graph neural networks for data-efficient and accurate interatomic potentials,” *Nature communications*, vol. 13, no. 1, p. 2453, 2022.
- [28] J. Gasteiger, J. Groß, and S. Günnemann, “Directional message passing for molecular graphs,” *arXiv preprint arXiv:2003.03123*, 2020.
- [29] D. Wang, R. Walters, X. Zhu, and R. Platt, “Equivariant q learning in spatial action spaces,” in *Conference on Robot Learning*. PMLR, 2022, pp. 1713–1723.
- [30] D. Wang, J. Y. Park, N. Sortur, L. L. Wong, R. Walters, and R. Platt, “The surprising effectiveness of equivariant models in domains with latent symmetry,” *arXiv preprint arXiv:2211.09231*, 2022.
- [31] A. K. Mondal, V. Jain, K. Siddiqi, and S. Ravanbakhsh, “Eqr: Equivariant representations for data-efficient reinforcement learning,” in *International Conference on Machine Learning*. PMLR, 2022, pp. 15908–15926.
- [32] B. Yu and T. Lee, “Equivariant reinforcement learning for quadrotor uav,” *arXiv preprint arXiv:2206.01233*, 2022.
- [33] X. Zhu, D. Wang, O. Biza, G. Su, R. Walters, and R. Platt, “Sample efficient grasp learning using equivariant models,” *arXiv preprint arXiv:2202.09468*, 2022.
- [34] D. Wang, R. Walters, and R. Platt, “SO(2)-equivariant reinforcement learning,” *arXiv preprint arXiv:2203.04439*, 2022.
- [35] D. Wang, M. Jia, X. Zhu, R. Walters, and R. Platt, “On-robot learning with equivariant models,” in *Conference on robot learning*, 2022.
- [36] P. J. Gorder and R. A. Hess, “Sequential loop closure in design of a robust rotorcraft flight control system,” *Journal of guidance, control, and dynamics*, vol. 20, no. 6, pp. 1235–1240, 1997.
- [37] K. T. Schütt, H. E. Sauceda, P.-J. Kindermans, A. Tkatchenko, and K.-R. Müller, “Schnet—a deep learning architecture for molecules and materials,” *The Journal of Chemical Physics*, vol. 148, no. 24, p. 241722, 2018.
- [38] A. Shankar, S. Elbaum, and C. Detweiler, “Freyja: A full multirotor system for agile & precise outdoor flights,” in *2021 IEEE International Conference on Robotics and Automation (ICRA)*. IEEE, 2021, pp. 217–223.